AIMS Mathematics, 5(4): 3256–3273.
DOI: 10.3934/math.2020209
Received: 10 March 2020
Accepted, 24 March 2020
Published: 27 March 2020

http://www.aimspress.com/journal/Math

Research article

Mathematical morphology approach to internal defect analysis of A356 aluminum alloy wheel hubs

Junsheng Zhang[1,2], Lihua Hao[1], Tengyun Jiao[1], Lusong Que[1] and Mingquan Wang[1,*]

[1] Science and Technology on Electronic Test and Measurement Laboratory, North University of China,Taiyuan 030051, China
[2] Department of Electronic engineering, Taiyuan Institute of Technology, Taiyuan 030008, China

*** Correspondence:** Email: wangmq@nuc.edu.cn.

Abstract: A356 aluminum alloy is a material widely used in the production of automobile wheels. Internal defects such as gas holes and shrinkage cavities are likely to develop in the process of low pressure casting. X-ray images of the hub are able to provide some information on such defects. This paper proposes a defect extraction method which is built on mathematical morphology. It involves three operations, i.e., the top-hat transform, the top-hat reconstruction transform and the dilation reconstruction. A larger square structuring element and a small threshold are used firstly to obtain all potential defect areas of the hub. A structuring element of a suitable size are applied to different defect areas in subsequent extraction. A new threshold is then decided to get the final defect extraction results. The experimental results show that the above defect extraction method not only works on X-ray hub images, but is robust against the interference caused by noises and hub geometry, and hence can potentially be extensively applied to X-ray detection of hubs.

Keywords: mathematical morphology; A356 aluminum alloy; automobile wheel hub; internal defect; X-ray testing
Mathematics Subject Classification: 93A30, 97M10

1. Introduction

The aluminum alloy wheel hub offers a number of advantages including low density and hence light weight, high thermal conductivity and hence quick heat dissipation, good formability, and

pleasing appearance, and is thus widely used in the automotive industry. A356 aluminum alloy is one of the most used materials in the making of automobile wheel hubs, during which the molten alloy liquid goes through low-pressure casting, T6 heat treatment and mechanical processing, until it turns into a finished product. To improve the quality of aluminum alloy hubs, scholars have made a lot of research covering billet preparation, melt temperature control, grain growth, mechanical properties, and fatigue life [1–5]. Despite all such efforts, in the production process, automobile wheels are always prone to some common casting defects such as gas holes, shrinkage cavities, shrinkage, and porosity [6]. X-ray non-destructive testing equipment then comes to play in defect detection [7]. In the X-ray examination of a hub, the radiation source radiates rays to the part to be examined, and the rays, after penetrating the examined part, are received by a flat panel detector behind. The received rays are then converted into a digital image, which is transferred to a computer. The radiation image, which carries the internal structure information of the hub, is then analyzed to determine the quality of the product [8].

Automatic detection of defects based on digital image processing makes a key step in X-ray examination of automobile hubs, and there have been a large amount of literature on this subject. The threshold segmentation algorithm, with the advantages of low computational cost and fast speed, has found extensive application in the field of defect detection in the auto industry [9–15]. X. Li successfully extracted the shrinkage cavities of a hub with the row-by-row adaptive thresholding algorithm [9]; Y. Tang proposes a maximum fuzzy exponential entropy criterion based on bound histogram, a threshold segmentation method built on fuzzy set theory, and enables fast and accurate separation of hub defects from the background [12]. J. Zhang proposes an algorithm combining dynamic threshold segmentation and morphological reconstruction, which allows accurate extraction of hub defects by setting the size of the smoothing operator window and the value of the threshold [15]. D. Merry uses an edge detection operator to process the hub image and get the preliminary detection result. Then, relying on area and mean gray, two quantities, to eliminate some pseudo-defects. Matching between and tracking of sequential images are performed on the remaining defects to produce the final detection result [16]. M. Carrasco, based on the fact that a physical hub defect is definable by geometries and is tractable across multiple images in an image sequence, develops a method that automatically detects the images of various parts of the hub supported by a technology of multiple viewpoints, which is able to detect true defects and eliminate most pseudo-defects [17]. A. Osman, drawing on the Dempster-Shafer data fusion theory, uses the measurement features of the examined hub as the information source and designs an automatic recognition function of defect type by use of a manually classified database, which improves the reliability of the hub examination [18]. X. Zhao uses grayscale arranging pairs (GAP) features to train the model on a series of images and then uses the trained model to extract the hub defects and design the Randomly Distributed Triangle (RDT) feature of the defects. A clarifier, called Sparse Representation-based Classification (SRC), is used to classify the defects. This method enables automatic recognition of weak and minor defects under low contrast and non-uniform illumination conditions [19,20]. Over recent years, with the advance of computer vision technology, some new methods have found application in automatic detection of wheel casting defects. An example in point is the convolutional neural network, a technology used in deep learning [21,22].

Mathematical morphology, originated in the 1960s, is used to analyze images by means of a small set, called structuring element, and has found wide application in the field of industrial

nondestructive examination [9,15,23]. In consideration of the fact that the internal defects of an aluminum alloy hub are much smaller than the overall hub size, this paper proposes a way that processes X-ray hub images by mathematical morphology through structuring elements of appropriate sizes, which is able to remove the geometries while maintaining the initial shapes of the defects. Then, the top-hat transform, the reconstruction transform and the fixed threshold binarization are used to extract the defects accurately.

2. Materials and method

2.1. X-ray testing of aluminum alloy hubs

Aluminum alloy wheel hubs are big, and their typical X-ray examination equipment consists of a radiation source, a detector, a controller and a protective lead room, as shown in Figure 1. The ray source includes a high-voltage power supply of 80 kV to 200 kV, from which X-rays are excited and penetrate through the examined part of the hub before being received by the detector. The received rays are converted into a visible light image, which is sent to a computer. Among the commonly used X-ray detectors are image intensifiers and flat panel detectors, the former mostly used for wheel hub examination in earlier days and requiring a CCD camera to digitize the X-ray images. Flat panel detectors are the most widely used in present-day hub examination systems, for they enable direct output of digital X-ray images. The source and detector are held together by a mechanism called C-arm which can tilt to a certain angle as directed by the controller so that different parts of the hub can be illuminated. Meanwhile, the controller also controls the forward movement and rotation of the hub ensuring that each hub part is examined. The protective lead room is provided to shield the X-rays and hold the complete set of equipment.

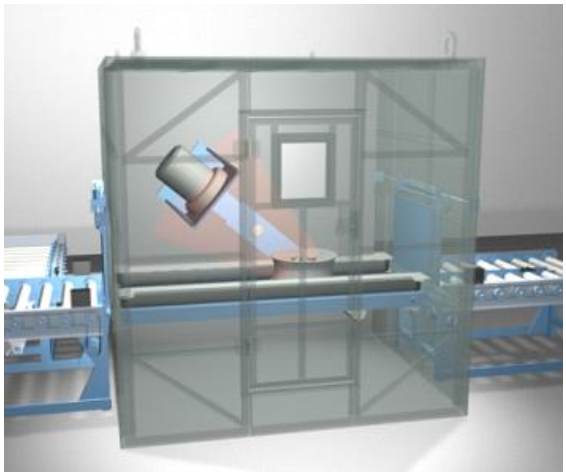

Figure 1. An X-ray examination system for hubs.

The voltage of the radiation source was set to 160 kV, the current to 2 mA. A flat panel detector with a resolution of 1024 × 1024 was used to receive the rays during the examination. An examination image is shown in Figure 2. As is clear in Figure 2, there is an obvious defect in the spoke of the hub, which should be extracted accurately by digital image processing.

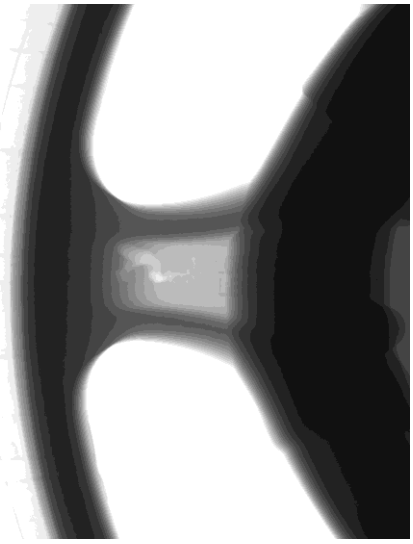

Figure 2. An X-ray image of the examined hub.

2.2. Introduction to mathematical morphology

Mathematical morphology was first proposed by Georges Matheron and Jean Serra, scholars at Paris School of Mines. Its basic idea is to analyze and detect the structures of images by means of customized structuring elements. This theory was initially limited to applications in the geometric analysis of binary images but later expanded to applications in the field of grayscale images and color images, to gradually develop into a very powerful nonlinear image analysis processing tool. The structuring element in mathematical morphology is generally much smaller than the image to be processed, and it is usually in the form of a binary matrix, the size of which represents the size of the structuring element and the range of pixels involved in the morphological operation. The center of the matrix is the origin of the structuring element, representing the corresponding target pixel in the morphological operation. A structuring element can take different shapes, such as square, circle, cross, etc., which is implemented by the elements, in the binary matrix, with a value of 1. In order to have a unique center, the size of the structuring element is generally set to an odd number. Figure 3 shows a square and a cross structuring element, both in 5×5 size, suggesting that 25 pixels are involved each time in the mathematical morphology operation. But for the square structuring element all the 25 pixels are used in the operation, while for the cross-shaped structuring element only the 9 pixels in the central row and the central column are used in the operation.

$$\begin{bmatrix} 1 & 1 & 1 & 1 & 1 \\ 1 & 1 & 1 & 1 & 1 \\ 1 & 1 & 1 & 1 & 1 \\ 1 & 1 & 1 & 1 & 1 \\ 1 & 1 & 1 & 1 & 1 \end{bmatrix} \qquad \begin{bmatrix} 0 & 0 & 1 & 0 & 0 \\ 0 & 0 & 1 & 0 & 0 \\ 1 & 1 & 1 & 1 & 1 \\ 0 & 0 & 1 & 0 & 0 \\ 0 & 0 & 1 & 0 & 0 \end{bmatrix}$$

(**a**) (**b**)

Figure 3. Structuring elements: (a) A square structuring element; (b) A cross structuring element.

For a digital image *f(x,y)*, when the origin of the structuring element B is on the pixel (x,y), there is an overlapping area between the structuring element and the image. A pixel in this overlapping area, after participating in the operation, generates a new gray value, which is assigned to (x,y) to complete an iteration of analysis. When all pixels are analyzed, a mathematical morphology operation is completed. Dilation and erosion are the basic operations in mathematical morphology. For an original image *f(x,y)* and structuring element B, dilation is mathematically defined as:

$$[\delta_B(f)](x,y) = \max_{(s,t)\in B}\{f(x+s,y+t)\} \tag{1}$$

The mathematical definition of erosion is:

$$[\varepsilon_B(f)](x,y) = \min_{(s,t)\in B}\{f(x+s,y+t)\} \tag{2}$$

The gray values of the corresponding pixel in dilation and erosion operations are the maximum and minimum, respectively, of the image in the window defined by the structuring element. For the entire image *f(x,y)*, dilation expands the bright area on the image, thus making the image brighter as a whole, so it works like a local maximum operator. Erosion, in contrast, shrinks the bright area on the image, making the image darker overall, so it is equivalent to a local minimum operator.

Opening and closing, too, are basic operations in mathematical morphology. They are a combination of erosion and dilation. The structuring element B, centered on the origin, is rotated 180 ° to form another structuring element, denoted by -B. The opening of the image *f(x,y)* is obtained through erosion of the image by B, followed by dilation of the resulting image by -B:

$$[\gamma_B(f)](x,y) = \delta_{-B}[\varepsilon_B(f)](x,y) \tag{3}$$

The closing of the image f(x,y) is obtained through dilation of the image by the structuring element B, followed by erosion of the resulting image by -B:

$$[\phi_B(f)](x,y) = \varepsilon_{-B}[\delta_B(f)](x,y) \tag{4}$$

In opening and closing operations, symmetrical structuring elements B and -B are used to erode and dilate the image, the result of the operations being independent of the origin of the structuring element itself. The opening attempts to restore the bright areas removed by the erosion operation. It sequentially performs the minimum value operation and the maximum value operation on image *f(x,y)* by the structuring element, with the final result that the bright areas on *f(x,y)* are completely removed, if they are smaller than B, while for the bright areas that are larger than B, only the portions unable to accommodate B are removed, leaving the other gray levels essentially unaffected. The closing operation attempts to recover the dark areas removed by dilation. It sequentially performs the maximum and the minimum operations on image *f(x,y)* by the structuring element, with the final result that the dark areas on *f(x,y)*, if they are smaller than B, are completely removed, while for the dark areas that are larger than B, only the portions unable to accommodate B are removed, leaving the other gray levels essentially unaffected.

In mathematical morphology, the top-hat transform is defined as the difference between the original image and the resulting image after opening:

$$[WHT(f)](x,y) = f(x,y) - [\gamma_B(f)](x,y) \tag{5}$$

The bright areas smaller than the structuring element B that have been removed by the opening operation are retained in the top-hat transform, while the other areas unaffected by opening cancel each other out in the subtraction process and therefore have a gray scale close to zero. By the top-hat transform, bright areas on image *f(x,y)* that are smaller than the structuring elements can be extracted, they generally corresponding to the target areas on the image.

Reconstruction is another major category in mathematical morphology and involves two input images: a marker image and a template image. The reconstruction operation is built on morphological geodesic dilation and geodesic erosion. Assuming there are a marker image, denoted by *f(x,y),* and a template image, denoted by *g(x,y),* both of the same size. When their gray values are $f \leq g$, the geodesic dilation with size of 1 is defined as:

$$\delta_g^1(f) = \delta_B^1(f) \wedge g \tag{6}$$

The symbol $\wedge$ in Eq. (6) represents a point-by-point minimum value operation, and the geodesic dilation is a point-by-point minimum between the template image and the marker image after the basic dilation, with the template image working to limit the spreading of the dilation of the marker image. The geodesic dilation of size n is obtained by performing n times of geodesic dilation on f with respect to g, as shown in Eq. (7):

$$\delta_g^{\mathrm{n}}(f) = \delta_g^1[\delta_g^{(n-1)}(f)] \tag{7}$$

When $f \geq g$, the geodesic erosion with size 1 and size n is defined respectively as:

$$\begin{cases} \varepsilon_g^1(f) = \varepsilon_B^1(f) \vee g \\ \varepsilon_g^{\mathrm{n}}(f) = \varepsilon_g^1[\varepsilon_g^{(n-1)}(f)] \end{cases} \tag{8}$$

The symbol $\vee$ represents a point-by-point maximum value operation, and the geodesic erosion is a point-by-point maximum between the template image and the marker image after the basic erosion, with the template image working to limit the shrinking of the erosion of the marker image. The geodesic transform of a given scale is rare in practical applications. However, when the scale is larger than 1 and begins to increase gradually, the dilation or shrinkage of the marker image, after a certain number of iterations, is completely blocked by the template image, and the geodesic transform becomes stable, hence leads to the concept of morphological reconstruction.

For a marker image f and a template image g of the same size (with $f \leq g$), the dilation reconstruction of g from f is defined as iterative geodesic dilations of f with respect to g until stability is achieved:

$$R_g^{\delta}(f) = \delta_{\mathrm{g}}^i(f) \tag{9}$$

where, i is the number of iterations when $\delta_{\mathrm{g}}^i(f) = \delta_{\mathrm{g}}^{i+1}(f)$. When $f \geq g$, the erosion reconstruction of g from f is defined as iterative geodesic erosions of f with respect to g until stability is achieved:

$$R_g^{\delta}(f) = \delta_g^i(f) \tag{10}$$

where, i is the number of iterations when $\varepsilon_g^i(f) = \varepsilon_g^{i+1}(f)$.

Morphological reconstruction, which does not call for any particular structuring element, demands a suitable pair of marker image and template image. The template image is generally the image to be processed, f; and the marker image can be obtained by various transformations of f. If the marker image is the resultant from the erosion of f and the template image is f itself, then the morphological dilation reconstruction is called the opening reconstruction of image f:

$$\gamma_R(f) = R_f^{\delta}[\varepsilon(f)] \tag{11}$$

The opening reconstruction preserves the shapes of the components in the image that have not been removed by erosion, removing only the image targets that are unable to accommodate the structuring element. The erosion reconstruction, with the image resulting from the dilation of the image f as the marker image, is called the closing reconstruction of f:

$$\phi_R(f) = R_f^{\varepsilon}[\delta(f)] \tag{12}$$

The closing reconstruction removes the areas that have disappeared completely in the dilation operation, but restores the areas that have been just affected by the dilation operation. Compared with the opening or closing, the opening or closing reconstruction is able to retain the rest details while removing the features smaller than the structuring element, and is hence widely used to filter image noises.

Subtracting the closing reconstructed image from the original image is called the top-hat reconstruction transform:

$$RWHT(f) = f - \gamma_R(f) \tag{13}$$

The top-hat reconstruction transform reconstructs the structural targets removed by the opening reconstruction, with the resulting image gray value always lower than what the corresponding top-hat transform gets. The dilation reconstruction of the top-hat transform from the top-hat reconstruction transform restores the target areas while removing the interference areas, hence helpful in accurately extracting hub defects.

2.3. Mathematical morphology analysis of local regions of the hub

A local region containing the defect is selected, as shown in Figure 4a, from the hub X-ray image shown in Figure 2 and analyzed from the perspective of the mathematical morphology discussed in Section 2.2. Hubs are complex in geometry and sometimes the grayscale features of the defects are similar to those of the structure itself. It may then prove difficult to separate the defects in an accurate way with the conventional image analysis approaches. Given the fact that defects are typically much smaller than the hub size, the top-hat transform can be used to extract such defects and then, in combination with the top-hat reconstruction transform, the dilation reconstruction is performed to highlight the hub defects while suppressing the hub geometry. The highlighted defects are extracted with the binarization method. Since the gray scale of the resulting image from the

top-hat transform or from the top-hat reconstruction transform is mostly close to 0, it is difficult to see the change in different regions before and after processing. Therefore, in this paper all the gray values are magnified by 3 when displaying the results of the top-hat transform, the top-hat reconstruction, and the dilation reconstruction, but the original gray values are used for analysis by the algorithm.

The top-hat transform is performed on Figure 4a using a square structuring element of 79×79, with the resulting image shown in Figure 4b. It can be seen that while the defect area is wholly extracted, some of the geometrical features of the hub are also extracted. The top-hat reconstruction is performed on Figure 4a, using the same structuring element, with the resulting image shown in Figure 4c, where the defect is extracted and a considerable amount of interference is removed. Now, with Figure 4c as the marker image and Figure 4b the template image, a dilation reconstruction is performed, and the resulting image is shown in Figure 4d. As seen in Figure 4d, the defect area is retained in its entirety and some of the interference areas are removed, bringing the defect area out more noticeably than in the original hub image seen in Figure 4a. Binarization with a fixed threshold is used to extract the defect area. The threshold is set to 11. The resulting image is shown in Figure 4e, from which it can be seen that the defect area is wholly extracted and the interference areas are removed. To present visually the accuracy of the defect segmentation region, the border of the defect area in Figure 4e is extracted and superimposed, in red line, on the original image, with the result shown in Figure 4f. As seen, the defect area in Figure 4a is accurately separated after a series of processing.

The choice of the structuring element and the setting of the fixed threshold make up the two key decisions in the above analysis process. To extract defects through the top-hat transform and the top-hat reconstruction transform, the structuring element used is generally an isotropic rectangle, the size of which should be slightly larger than the defect area, because too small a structuring element is unable to completely extract defects, while too large a structuring element makes it hard to suppress the geometry interference of the hub. If the square structuring element is reduced from 79×79 to 39×39, the top-hat transform and the top-hat reconstruction on the image in Figure 4a produce the results shown in Figure 5a and 5b respectively, which, after the dilation reconstruction, produce a result shown in Figure 5c. In contrast to the corresponding image in Figure 4, it can be seen that the result obtained by a smaller structuring element is lower in gray value, both the interference area and the defect area getting smaller. If the defect is extracted using the same threshold value 11, the segmentation result when superimposed on the original image is as shown in Figure 5d, where it can be seen that only a part of the defect area is extracted.

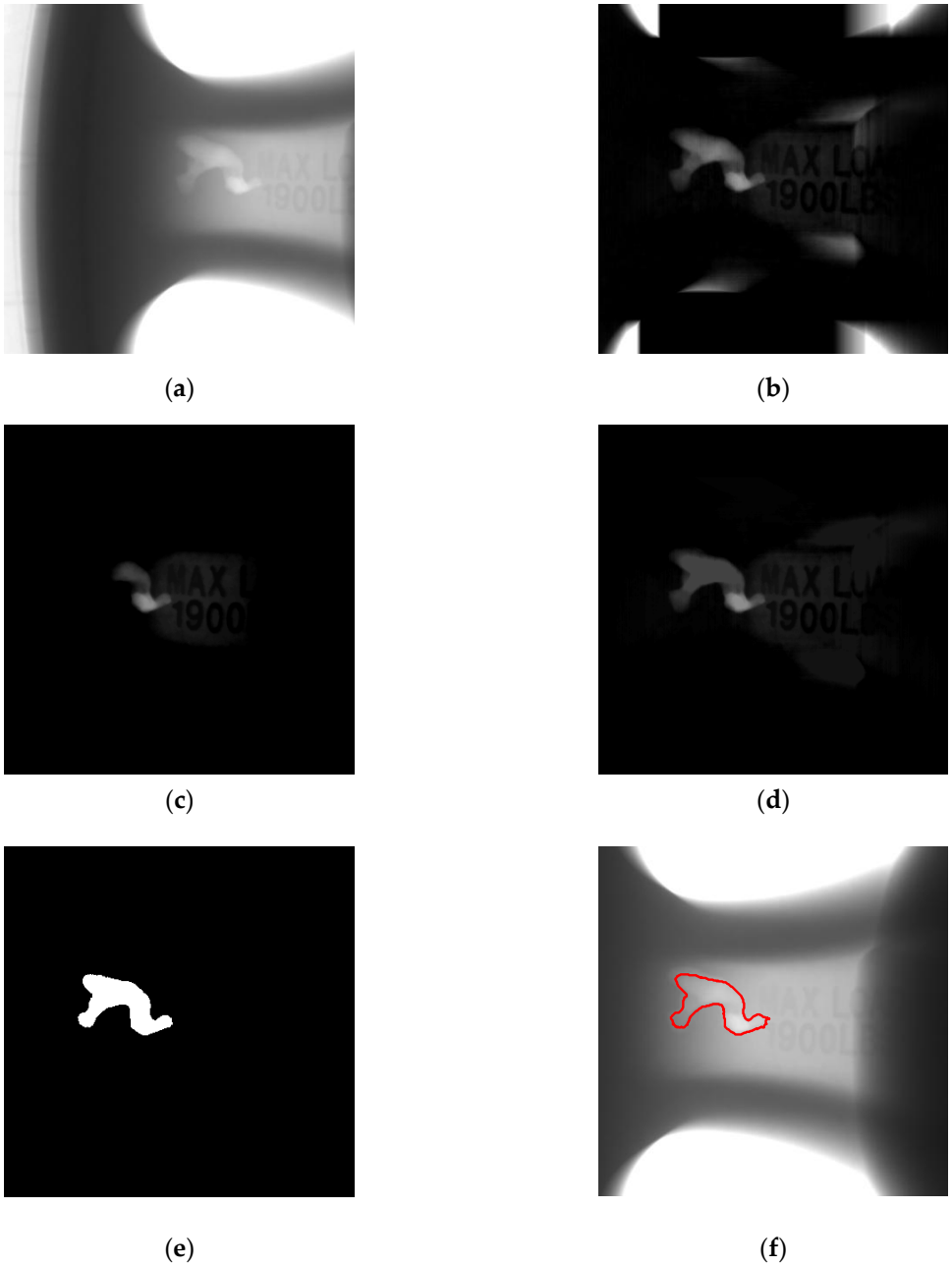

Figure 4. Results of mathematical morphology analysis: (a) original image; (b) result of Top-hat transform with square structuring element of 79 × 79; (c) result of Top-hat reconstruction with the same structuring element; (d) result of dilation reconstruction; (e) binarization result with a fixed threshold of 11; (f) superimposed result of defect segmentation.

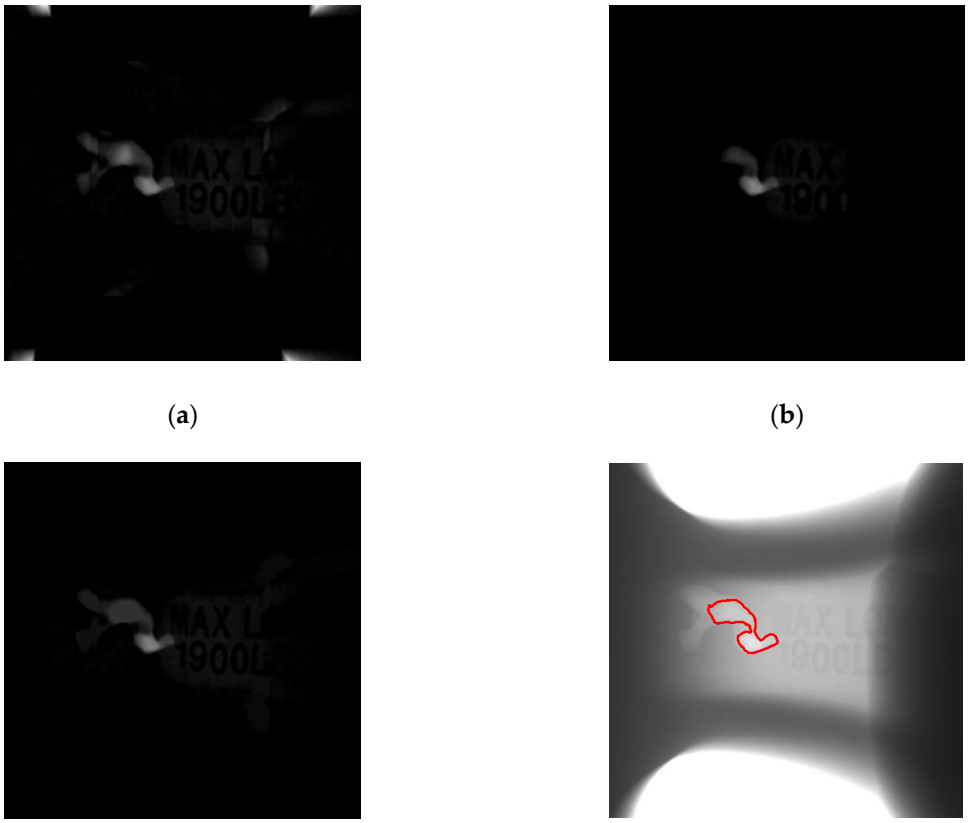

(**a**) (**b**)

(**c**) (**d**)

Figure 5. Results using structuring element of 39 × 39: (a) result of Top-hat transform; (b) result of Top-hat reconstruction; (c) result of dilation reconstruction; (d) superimposed result of defect segmentation by threshold 11.

Too large a structuring element can likewise cause interference in defect extraction. If the square structuring element is enlarged from 79 × 79 to 109 × 109, the top-hat transform on the image in Figure 4a produce the result shown in Figure 6a, which, after the top-hat reconstruction transform, produces a result shown in Figure 6b. The dilatation reconstruction results of the two are given in Figure 6c, and when a threshold of 11 is applied the extracted defect is as shown in Figure 6d as marked. It can be seen that an unduly large structuring element brings interference to the structural area, apart from driving up the amount of computation, and is hence disadvantageous for accurate extraction of the hub defects.

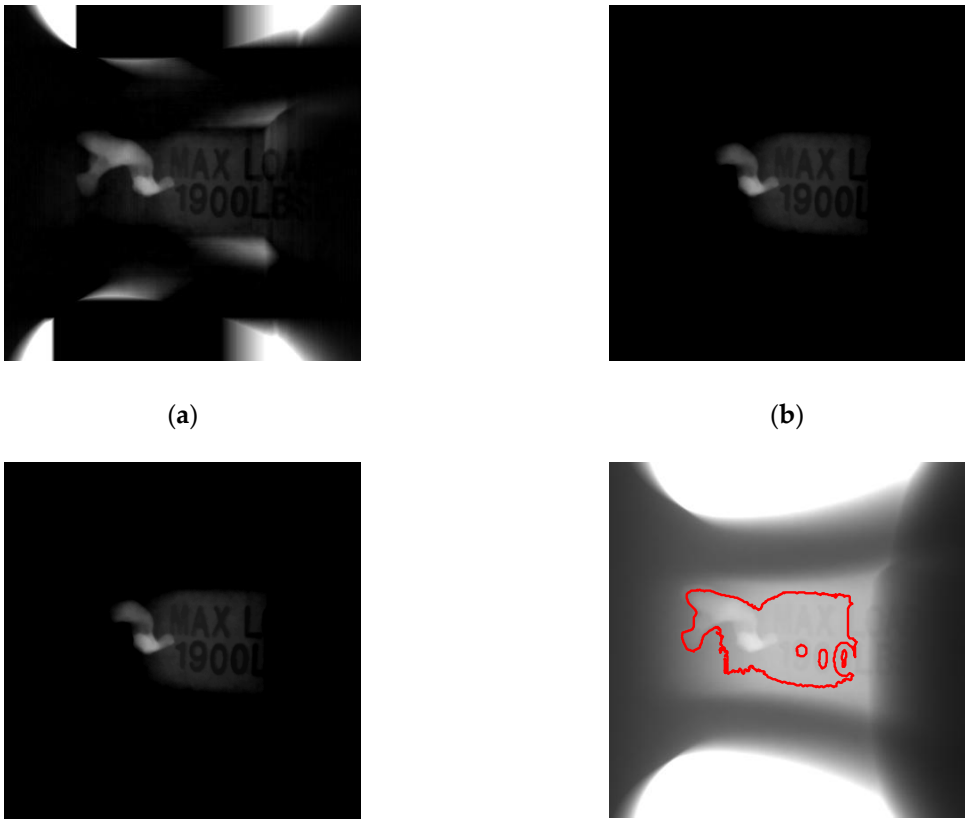

(**a**) (**b**)

(**c**) (**d**)

Figure 6. Results using structuring element of 109 × 109: (a) result of Top-hat transform; (b) result of Top-hat reconstruction; (c) result of dilation reconstruction; (d) superimposed result of defect segmentation by threshold 11.

Setting a fixed threshold makes up the last while the most important step in defect extraction. Different threshold values for Figure 4d produce different segmentation results. Figure 7a and 7b show the marked segmentation result when the threshold is set to 4 and 12 respectively. It can be seen that with a too small threshold, more interference areas that have not been removed in the morphological operation will be retained and for a too large threshold, the extraction of the defect area is incomplete. When the size of the structuring element varies, choosing a different fixed threshold can produce a better segmentation effect. For example, when the threshold is set to 7 in Figure 5c, the segmentation result shown in Figure 7c is obtained. Compared with Figure 5d, it has made a notable improvement in defect extraction, though with a small interference. In a similar way, when the threshold for Figure 6c is set to 19, the marked defect result in Figure 7d is obtained, where the interference drops remarkably and, essentially, the defect area is extracted accurately.

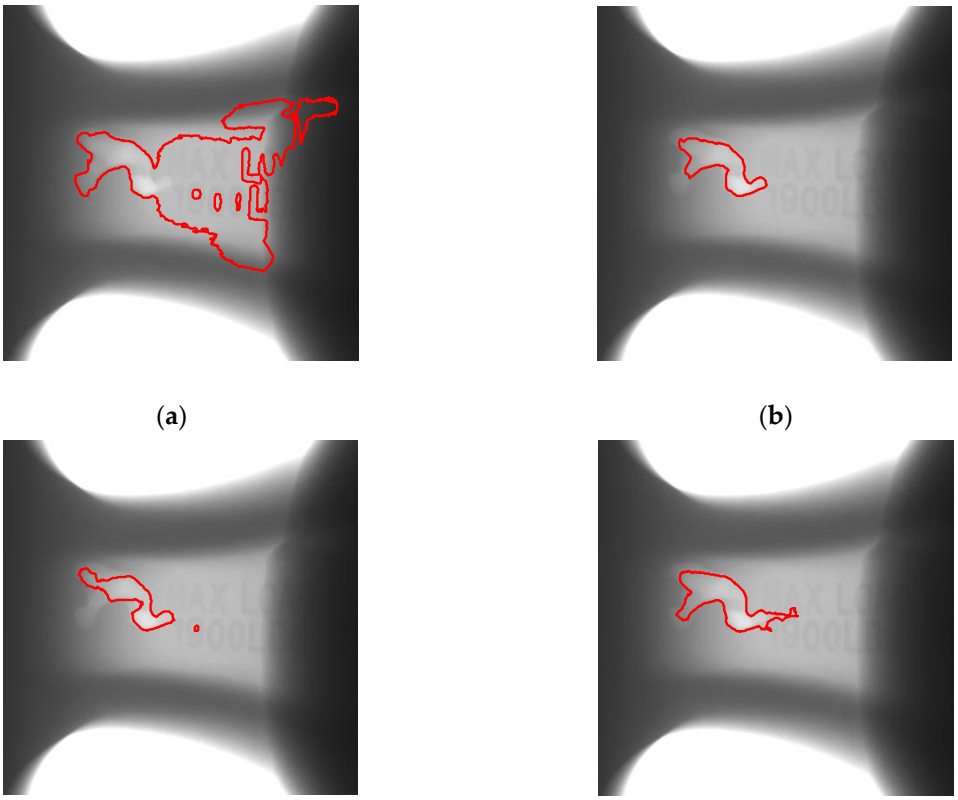

(**a**) (**b**)

(**c**) (**d**)

Figure 7. Results using different thresholds and structuring elements: (a) result of threshold 4 and structuring elements of 79 × 79; (b) result of threshold 12 and structuring elements of 79 × 79; (c) result of threshold 7and structuring elements of 39 × 39; (d) result of threshold 7 and structuring elements of 109 × 109.

2.4. Mathematical morphology analysis process of hub X-ray images

As discussed in Section 2.3, in morphological extraction of hub defects, the size of the structuring element plays a critical role, for it not only determines whether defects can be highlighted from the hub geometry, but also influences the determination of the subsequent fixed threshold value. Internal defects of hubs vary greatly in type and because of this a single fixed-size structuring element is unable to work well with all defects. Manually determining the size of structuring elements is not much feasible in practical applications. Hence, finding an automatic way to determine a structuring element of proper size becomes a core task in morphological analysis of internal hub defects.

However, considering today's art of the hub manufacturing, the internal defects cannot be too large and there must be an upper limit to a defect size. After analyzing a variety of hub X-ray images, it is noticed that the height or width of the image can serve as a reference for the selection of the structuring element size. With a hub image of, say, 1024 × 1024, a structuring element of about 10% the image size, or, 101 × 101 is able to reveal all defects, after which a smaller threshold value helps to extract all potential defect areas. These potentially defective areas may contain the geometry of the hub itself, similar to the local area used in Section 2.3, which demands a smaller structuring element to bring out the real defects. Potential defect areas vary one from another in size. The shorter

dimension of the circumscribed rectangle of a defect works well as a reference for determining the size of the structuring element. After that, the morphological analysis is performed and a greater threshold is used to make defect segmentation, which is able to produce satisfactory results.

From the above analysis, a hub defect segmentation process as follows is proposed:

1. Find the height and width of the X-ray image of the hub. With 10% of the smaller dimension as a reference, construct an appropriately-sized square structuring element for the top-hat transform, the top-hat reconstruction transform, and the dilation reconstruction, to get the preliminary separation results of the hub defects;
2. Use a smaller threshold to binarize the preliminary separation results, which produces potential defect areas;
3. Construct a square structuring element of a size 50% of the smaller dimension of the circumscribed rectangle of each potential defect area, and then perform the top-hat transform, the top-hat reconstruction transform, and the dilation reconstruction on each of the potential defect areas, which produces the final separation results of the defects;
4. Use a larger threshold to binarize the final separation results, which produces the final segmentation results of the hub defects.

In this segmentation process, Step 2 and 4, in particular, involve different thresholds to obtain the final results of the mathematical morphology analysis. Step 2, to make certain that all the defect areas are extracted, typically opts for a small threshold; Step 4, on the other hand, generally uses a larger threshold in order to eliminate as much interference as possible.

3. Experiment results

The data used in this experiment came from the on-line detection system of hub defects described in Section 2.1. The X-ray image used in the analysis has a resolution of 1024×1024. Taking Figure 2 as the object to be processed, perform Step 1 of the segmentation process using a square structuring element of 101×101, with the resulting image as shown in Figure 8a, in which most of the structural areas of the hub itself are removed, and the defect is brought out. With a threshold of 1, the binarization produces an image as shown in Figure 8b. A circumscribed rectangle is superimposed on the original image, as shown in Figure 8c. Obviously from Figure 8c, the red rectangle delineates the potential defect area, and the green one identifies the area as the geometry of the hub itself. Construct a square structuring element of a size half the smaller dimension of the red rectangle, and perform the top-hat transform, the top-hat reconstruction transform, and the dilation reconstruction on the area enclosed by the red rectangle in Figure 8c; construct a square structuring element of a size half the smaller dimension of the green rectangle, and perform the top-hat transform, the top-hat reconstruction transform, and the dilation reconstruction on the area marked by the green rectangle. The results of the operations are the second mathematical morphology analysis results of the hub X-ray image, which are multiplied with Figure 8b, the binarization result of the first analysis, to produce the result as shown in Figure 8d. A comparison between Figure 8a and Figure 8d shows that after the second mathematical morphology analysis, the structural interference area, marked by the green rectangle, is eliminated, retaining only the area containing the defect. With a threshold of 12, binarization is performed on Figure 8d, to produce what is shown in Figure 8e, which is then superimposed on the original image, as shown in Figure 8f. The result produced by following the defect analysis process is obviously in consistence with what is obtained

from manual determination of the local area described in Section 2.3. Hence, the proposed process works well in analyzing hub defects.

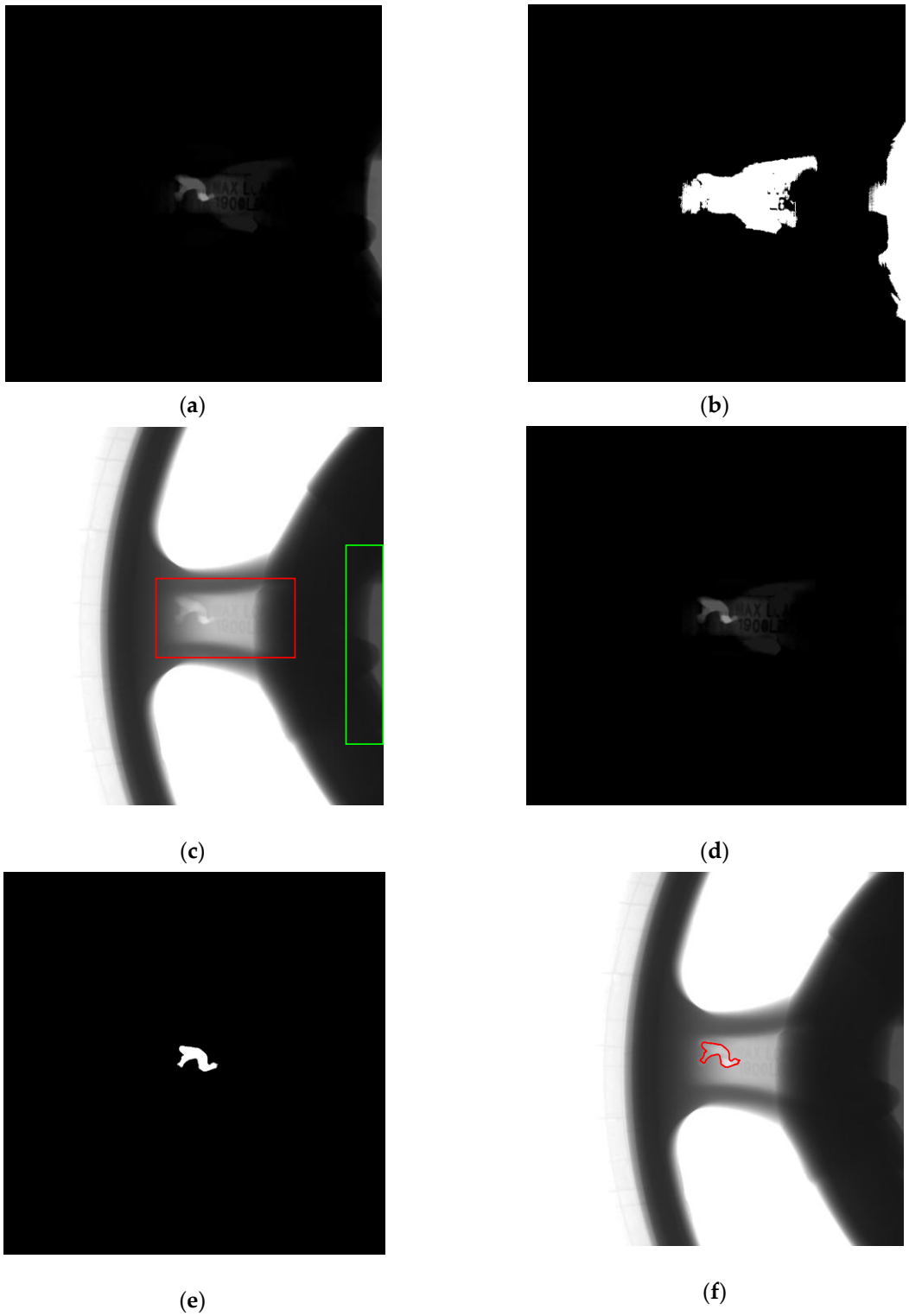

Figure 8. Segmentation result of proposed method: (a) preliminary separation result of image; (b) binarization result with a threshold of 1; (c) circumscribed rectangle of binarization result; (d) final separation result of image; (e) final segmentation result of defect; (f) superimposed result of proposed method.

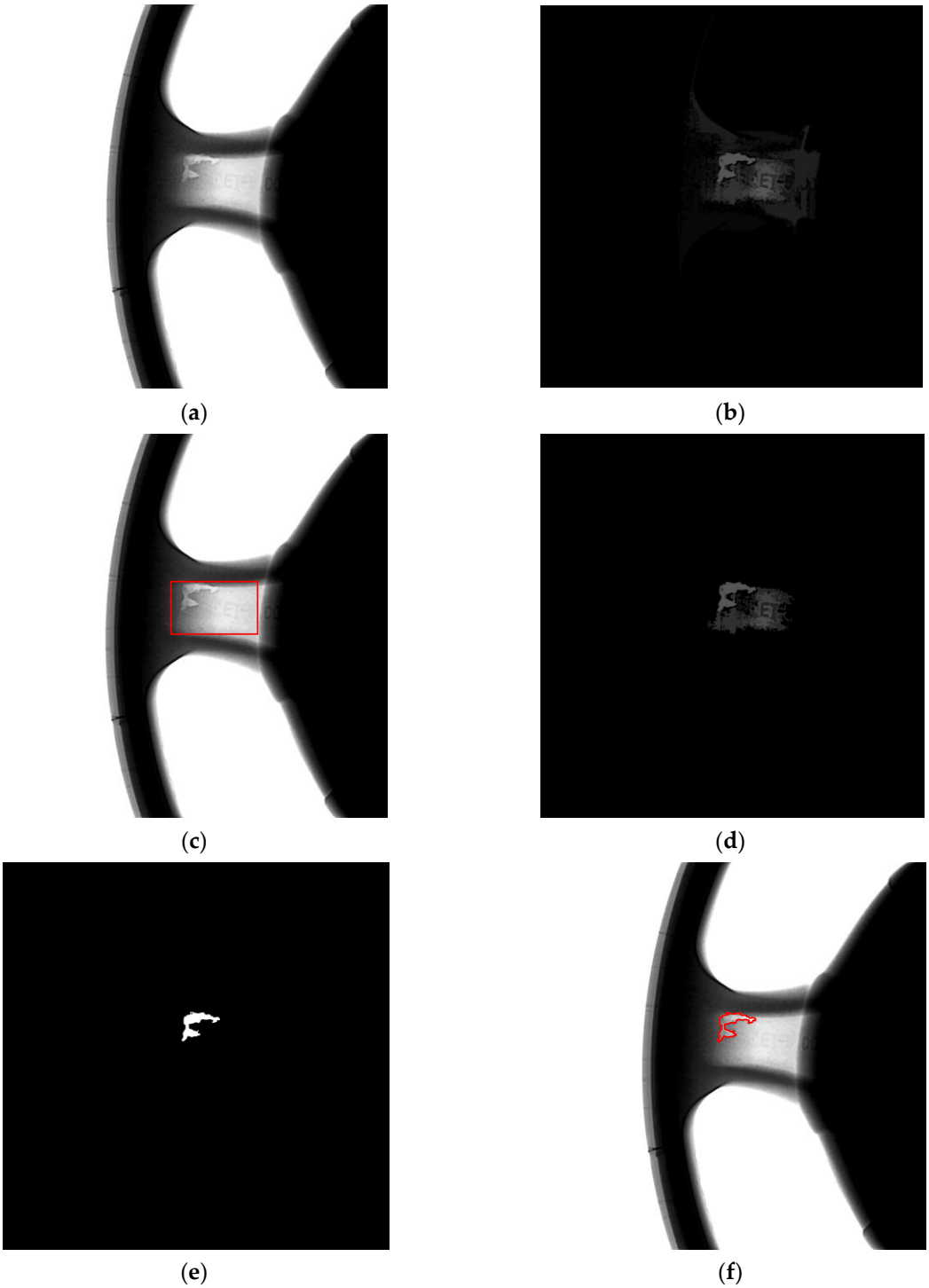

Figure 9. Another result of proposed method: (a) original image; (b) preliminary separation result of image; (c) circumscribed rectangle of segmentation result with a threshold of 11; (d) final separation result of image; (e) final segmentation result of defect; (f) superimposed result of proposed method.

Figure 9a shows an X-ray image of another hub acquired by the same acquisition system, and it can be noted that the spoke portion has a defect too. With the same parameters, that is, using a square structuring element of 101×101 for the top-hat transform, the top-hat reconstruction transform, and

the dilation reconstruction, the preliminary separation result of the hub defect is as shown in Figure 9b; using a threshold value of 11 for binarization, and the corresponding circumscribed rectangle is as shown in Figure 9c. Construct a square structuring element of half the smaller dimension of the circumscribed rectangle and perform Step 3 of the segmentation process within the scope delimited by the binarization of a threshold value of 11, to get the resulting image shown in Figure 9d. With a larger threshold of 27, the resulting defect segmentation is as shown in Figure 9e, which is transferred to the original image as shown in Figure 9f.It can be seen that the same defect segmentation process works equally on different wheel images.

4. Discussion

From the experimental results in the third section it can be seen that the proposed defect extraction process works with equal effectiveness on different hub images, and the defects areas can be identified accurately if parameters are assigned proper values. A total of four parameters are involved in the segmentation process: the size of the structuring element and the threshold for preliminary extraction of the defect areas, and those for final extraction of the defect areas. The effect of their values on the defect extraction is discussed in Section 2.3. For different hub images, the size of the structuring element can be determined based on the size of the image and the area. There is not a single rule for selecting the threshold value, and the choice depends on the image itself. For example, the threshold values of 1 and 12 are used for Figure 8, or 11 and 27 for Figure 9. In actual hub defect detection, hubs of the same model typically are examined using a same set of parameters, including the voltage and current of the radiation source, the imaging method for different parts, etc. These parameters determine the quality of the X-ray image of the hub and, in an indirect way, determine the setting of the threshold value. The operator can tune the parameters to arrive at the optimal setting and keep to it until the whole batch of the hubs are examined.

5. Conclusion

This paper proposes a solution to extract internal defects of hubs by mathematical morphology operations that involve top-hat transform, top-hat reconstruction transform and dilation reconstruction, as a way to simplify the image and remove most of the interference while retaining and highlighting the defect areas. A fixed threshold is then used to bring out the internal defects accurately. The top-hat transform works to extract bright areas smaller than the structuring element, which inevitably creates geometry interference as well as brings out the defects. The top-hat reconstruction transform causes less geometry interference than the top-hat transform, but may extract incomplete defect areas. The proposed method combines the top-hat transform and the top-hat reconstruction transform in the dilation reconstruction operation, which makes full use of their respective advantages while avoiding their shortcomings, hence achieving the purpose of simplifying the gray scale of the hub image. It lays a good foundation for the threshold segmentation of defects. Another innovation of the proposed method is the automatic sizing of the structuring element. By analyzing the present manufacturing process and the inspection process of hubs, a larger structuring element is set based on the height or width of the X-ray image, to extract preliminarily a potential defect area. Then, construct a circumscribed rectangle of the potential defect area and create a small structuring element based on the smaller dimension of the rectangle, hence automating the

setting of the structuring elements, which improves the accuracy in morphological separation of defects. Finally, the method described in this paper designs a reasonable defect extraction process, which first extracts potential defect areas using a large structuring element and a small threshold, and then extracts each of the defects using a large threshold and a structuring element of self-adjusted size, thus enabling accurate extraction of the internal defects in different hubs.

Acknowledgments

This work was supported in part by Key Research and Development (R&D) Projects of Shanxi Province (No. 201803D121069), and National Special Project for the Development of Major Scientific Instruments and Equipment of China (No. 2013YQ240803), and Scientific and Technological Innovation Programs of Higher Education Institutions in Shanxi Province (No. 2013163).

Conflict of interest

All authors declare no conflicts of interest in this paper.

References

1. P. Li, D. M. Maijer, T. C. Lindley, et al. *Simulating the Residual Stress in an A356 Automotive Wheel and Its Impact on Fatigue Life*, Metall. Mater. Trans. B, **38** (2007), 505–515.
2. S. Wang, N. Zhou, W. Qi, et al. *Microstructure and mechanical properties of A356 aluminum alloy wheels prepared by thixo-forging combined with a low superheat casting process*, T. Nonferr. Metal. Soc., **24** (2014), 2214–2219.
3. N. K. Kund, P. Dutta, *Numerical study of influence of oblique plate length and cooling rate on solidification and macrosegregation of A356 aluminum alloy melt with experimental comparison*, J. Alloy. Compod., **678 (**2016), 343–354.
4. L. Ming, Y. Li, G. Bi, et al. *Effects of melt treatment temperature and isothermal holding parameter on water-quenched microstructures of A356 aluminum alloy semisolid slurry*, T. Nonferr. Metal. Soc., **28** (2018), 393–403.
5. P. Fan, S. Cockcroft, D. Maijer, et al. *Examination and Simulation of Silicon Macrosegregation in A356 Wheel Casting*, Metals, **8** (2018), 503.
6. B. Zhang, S. L. Cockcroft, D. M. Maijer, et al. *Casting defects in low-pressure die-cast aluminum alloy wheels*, JOM, **57** (2005), 36–43.
7. H. Boerner, H. Strecher, *Automated X-Ray Inspection of Aluminum Castings*. IEEE T. Pattern Anal., **10 (**1988), 79–91.
8. D. Mery, T. Jaeger, D. Filbert, *A review of methods for automated recognition of casting defects*, Insight, **44** (2002), 428–436.
9. X. Li, S. K. Tso, X. Guan, et al. *Improving Automatic Detection of Defects in Castings by Applying Wavelet Technique*, IEEE T. Ind. Electron., **53** (2006), 1927–1934.
10. T. Saravanan, S. Bagavathiappan, J. Philip, et al. *Segmentation of defects from radiography images by the histogram concavity threshold method*, Insight, **49 (**2007), 578–584.

11. Y. Wang, Y. Sun, P. Lv, et al. *Detection of line weld defects based on multiple thresholds and support vector machine*, NDT E Int., **41 (**2008), 517–524.
12. Y. Tang, X. Zhang, X. Li, et al. *Application of a new image segmentation method to detection of defects in castings*, Int. J. Adv. Manuf. Technol., **43 (**2009), 431–439.
13. X. Yuan, L. Wu, Q. Peng, *An improved Otsu method using the weighted object variance for defect detection*, Appl. Surf. Sci., **349** (2015), 472–484.
14. M. Malarvel, G. Sethumadhavan, P. C. R. Bhagi, et al. *An improved version of Otsu ' s method for segmentation of weld defects on X-radiography images*, Optik, **142** (2017), 109–118.
15. J. Zhang, Z. Guo, T. Jiao, et al. *Defect Detection of Aluminum Alloy Wheels in Radiography Images Using Adaptive Threshold and Morphological Reconstruction,* Appl. Sci., **8** (2018), 2365.
16. D. Mery, D. Filbert, *Automated flaw detection in aluminum castings based on the tracking of potential defects in a radioscopic image sequence*, IEEE Trans. Robot. Autom., **18** (2002), 890–901.
17. M. Carrasco, D. Mery, *Automatic multiple view inspection using geometrical tracking and feature analysis in aluminum wheels*, Mach. Vis. Appl., **22** (2011), 157–170.
18. A. Osman, V. Kaftandjian, U. Hassler, *Improvement of x-ray castings inspection reliability by using Dempster –Shafer data fusion theory*, Pattern Recogn. Lett., **32** (2011), 168–180.
19. X. Zhao, Z. He, S. Zhang, *Defect detection of castings in radiography images using a robust statistical feature*, J. Opt. Soc. Am. A, **31** (2014), 196–205.
20. X. Zhao, Z. He, S. Zhang, et al. *A sparse-representation-based robust inspection system for hidden defects classification in casting components*, Neurocomputing, **153** (2015), 1–10.
21. D. Mery, C. Arteta, *Automatic Defect Recognition in X-ray Testing using Computer Vision*. In: Proceedings of the 2017 IEEE Winter Conference on Applications of Computer Vision (WACV), Santa Rosa, CA, USA, March 2017, 24–31.
22. J. Lin, Y. Yao, L. Ma, et al. *Detection of a casting defect tracked by deep convolution neural network*, Int. J. Adv. Manuf. Technol., **97** (2018), 573–581,
23. R. Alaknanda, S. Anand, P. Kumar, *Flaw detection in radio-graphic weld images using morphological approach*, NDT E Int., **39** (2006), 29–33.

AIMS Press